# Multifunctional and tunable metastructure based on VO$_2$ for polarization conversion and absorption

YUPENG LI,[1] LI ZENG,[1] HAIFENG ZHANG,[1,*] DAN ZHANG,[2] KE XIA,[1] AND LEI ZHANG[1]

[1]*College of Electronic and Optical Engineering & College of Flexible Electronics (Future Technology), Nanjing University of Posts and Telecommunications, Jiangsu province 210023, China*
[2]*College of Information Science and Technology, Nanjing Forestry University, Nanjing 210023, China*
*hanlor@163.com

**Abstract:** The design of tunable and multifunctional metastructures (MSs) is currently a trend in the terahertz (THz) field. Based on the characteristic that thermal excitation can cause the phase transition of vanadium dioxide (VO$_2$), a MS that concentrates both cross-polarization conversion and absorption functions is proposed in this paper, and switching two functions can be achieved by controlling the temperature. At high temperatures (68°C), the proposed MS exhibits a narrow-band absorption function in the range of 0.67 THz-0.95 THz. When the temperature drops below 68°C, VO$_2$ is in the insulated state, and the structure can be considered as a polarization converter. Simulation results indicate that the broadband cross-polarization conversion can be realized in 0.69 THz-1.38 THz with a polarization conversion ratio above 90% and a relative bandwidth of 66.7%. This paper analyzes the amplitude, phase, and surface current distributions under the polarization conversion function, as well as the impedance, power loss distributions, and equivalent circuits under the absorption function. In addition, the angular stability and the influences of the structural parameters on performance are also discussed. The proposed MS is suitable for complex applications due to its tunability and dual functionality.

## 1. Introduction

With the rapid development of science and technology, the use of electromagnetic waves is becoming increasingly common. However, electromagnetic interference risks daily communication, various electronic devices, and even human health to a certain extent. Therefore, the research on the absorbers is of strategic importance. Applying the absorption material in the electromagnetic shielding and electromagnetic protection [1] is gradually gaining attention. Wave absorption structures are the functional materials that reduce the intensity of the reflected electromagnetic waves (EMW) by absorbing the incident EMW. Besides, the absorbers can further improve the target's stealth performance by reducing its radar scattering cross-section [2]. The phenomenon in which the amplitude and direction of the electric field for EMW are changed with time at arbitrary points in space is called the polarization of EMW, which is widely used in antenna radiation [3], radar detection [4], optical devices [5], communication systems [6] and other fields. For example, the radiation from most antennas, such as dipoles and butterfly antennas [7], is generally characterized by a strong orientation, so the device receiving the signal is highly selective concerning the polarization state. In short, the device that can convert the polarization state for the EMW is known as the polarization converter. The conventional absorbers and polarization converters are challenging to be used widely due to the disadvantages of poor stability, heaviness, thickness, *etc*. So, the focus of the research move on the absorbers and polarization converters, which are stable, lightweight, and can be quick to miniaturize and integrate.

Metastructures (MSs) whose applications are essentially the same as metasurfaces are offshoots and 3D extensions of metasurfaces [8]. The emergence of MSs is due to the increasing number of multilayer structures caused by the escalation of application requirements; so the conventional metasurfaces which are used to define 2D systems are no longer suitable for defining 3D structures. MSs feature extraordinary physical properties, such as the negative refractive index and the negative dielectric constant [9], which are not present in natural materials. By the specific design of the MS unit, the control in both phase and amplitude of EMW can be achieved, resulting in polarization conversion, absorption, *etc*. Numerous MSs that can perform polarization conversion or wave absorption functions have been developed recently. In 2018, a polarization converter can convert the linear polarized EMW to the circular polarized EMW with an axial ratio (AR) below 3 dB in the band from 2.98 GHz to 3.16 GHz proposed by Akgol *et al* [10]. Besides, Chen *et al*. [11] designed a periodic cylindrical array based on InSb material with a highly thermosensitive relative permittivity in 2020. High sensing performance can be obtained at room temperature (300 K) with 99.9% absorptivity at 1.90 THz for the above structure. Moreover, in 2021, the MS with the linear-to-circular polarization conversion in both 15.0 GHz-21.2 GHz (34.3%) and 27.0 GHz-30.3 GHz (11.5%) where AR can be maintained below 3 dB [12] was presented.

Increasingly, attention is placed on designing multifunctional MSs to meet the needs of more sophisticated applications. A MS was designed by Dutta *et al*. [13] in 2021, enabling both the cross- and the linear-to-circular polarization conversion in the multiple operating bands. Besides, more controllable materials and devices are also used in designing multifunctional MSs. In 2020, Li *et al*. [14] introduced a MS containing the PIN diode whose function can be switched from perfect transparency to excellent absorption by controlling the external voltages applied across the diodes. Liu's team [15] achieved both cross-polarization conversion (36.9 THz-38.8 THz) and linear-to-circular polarization conversion (35.8 THz and 39.9 THz) on a MS by regulating the Fermi energy of graphene in 2021. In the same year, Zhang *et al*. [16] also used graphene to design a cross-shaped resonant surface and its complementary MSs structure to achieve the abovementioned functions. The multifunctional and tunable MSs overcome the disadvantages of conventional MSs, such as limited functionality and the single working band, which provide the flexibility to adapt to the complicated and constantly evolving communication environment.

Meanwhile, as the research into phase transition materials continues, the advantages of vanadium dioxide ($VO_2$) in designing multifunctional devices are coming to the fore. Generally speaking, when the temperature is below 68°C, $VO_2$ with the monoclinic lattice structure presents the insulating or the semiconducting state, measured by the conductivity. When the temperature exceeds 68°C, the arrangement of $VO_2$ is transformed into the tetragonal rutile structure while the state turns to the metallic phase [17–19]. As the phase transition material, the phase transition temperature of $VO_2$ is relatively low and is easily reached by the thermostats. In addition, $VO_2$ also possesses the advantages of being chemically stable and having a high resistance temperature coefficient at room temperature [20]. However, the above process is reversible for the phase change of $VO_2$ by thermal excitation [21], which is significant for the tunability and versatility of the MSs. Recently, tunable and multifunctional MSs based on the phase transition characteristic of $VO_2$ have emerged. For example, in 2020, a $VO_2$-based MS that can simultaneously perform absorption and linear-to-circular polarization conversion functions was proposed [22]. Qiu et al. also designed a MS [23] with broadband absorption, linear-to-linear polarization conversion, and linear-to-circular polarization conversion functions. A $VO_2$-graphene-based MS [24] can also be bi-functional simultaneously, except that the process is complex to simultaneously conditioning vanadium dioxide and graphene. More, there is the MS with the asymmetric transmission and the bidirectional absorption switchable in the terahertz, the MS with the functions of both absorption and electromagnetically induced transparency, the MS that can switch between broadband and narrowband absorption, and simultaneous realizations of the absorber and transparent conducting metal in a single MS [25]. In addition, $VO_2$ also shows potential applications in various fields

such as intelligent windows [26], photocatalysis [27], memristor MSs [28], and infrared thermal imaging [28].

Different from the functions mentioned above that can be achieved on a MS, in this work, a tunable multifunctional MS that enables the functions of polarization conversion and wave absorption is proposed based on the phase transition characteristics of $VO_2$. When $VO_2$ is at a high temperature, the proposed MS absorbs 90% and more of the EMW in the range of 0.67 THz-0.95 THz. In this case, the design consists of two circular structures with staggered slots in metal and $VO_2$, a $VO_2$ rectangular resonant patch with the "T" shaped slotted structures, three layers of the dielectric substrate, and a metal reflector. As the temperature decreases, the $VO_2$ structures cease to resonate, and the function of the MS switches from the absorption to the polarization conversion of EMW. At this point, the proposed MS achieves the polarization conversion ratio (PCR) above 0.9 in the range of 0.69 THz-1.38 THz, with a relative bandwidth (*RB*) of 66.7%. The multifunctional MS holds potential for intelligent applications and complex environments in the terahertz (THz) frequency region.

## 2. Theoretical model

The detailed schematic views of the proposed MS unit from various angles are provided in Fig. 1. The periodically arranged $(3 \times 3)$ array diagram is depicted in Fig. 1(a), demonstrating certain information regarding the incident waves. Figs. 1(b) and (c) show the side view and the structural decomposition of the unit separately. This MS unit generally comprises three layers of resonant patches and a metal reflector plate, separated by three dielectric substrate layers with different thicknesses. The material used for the dielectric substrate is Polyimide, which possesses a dielectric constant value of 3.5 [29]. Gold with a conductivity of $4.561 \times 10^7$ S/m [30] is used in the top resonant patch and the metal reflector at the bottom, displayed in red in Fig. 1. The $VO_2$ resonant patches whose conductivity can rise from 20 S/m (296 K) to $1 \times 10^5$ S/m (341 K) [31–33] with increasing temperature are indicated in blue. Figure 1(c) presents more visual details about the resonant patches. A circular structure with three staggered slots along the *u*-axis forms the metal resonant patch at the top of the unit. The $VO_2$ resonant patch adjacent to the above resonant patch differs merely in direction of the slots, which is deflected from the *u*-axis to the *v*-axis. In other words, the $VO_2$ circular resonant patch can be obtained when the metal resonant patch is rotated 90° clockwise. The third resonant patch on such a MS is formed by combining five rectangular patches collectively, each of which features four "T" shaped slotted structures in different orientations. It is worth noting that the rectangular patch placed in the middle is proportional to the four rectangular patches located at its four corners in size. Further details on the structural parameters are listed in Table 1.

**Table 1. Detailed parameters and values of the proposed MS**

| Parameters | $r_1$ | $w_1$ | $w_2$ | $a$ |
|---|---|---|---|---|
| Value (μm) | 25 | 5 | 15 | 3 |
| Parameters | $b$ | $p$ | $l_1$ | $l_2$ |
| Value (μm) | 10 | 60 | 28 | 6 |
| Parameters | $t_1$ | $t_2$ | $t_3$ | $h$ |
| Value (μm) | 1 | 28 | 4 | 0.2 |
| Parameters | $k_1$ | $k_2$ | | |
| Value | 0.56 | 0.45 | | |

The modeling and calculations for the proposed MS are performed in HFSS, a commercial 3D structural electromagnetic field simulation software. In the simulation, it is necessary to construct the arrangement of the boundless period, which is accomplished by setting the Master-Slave
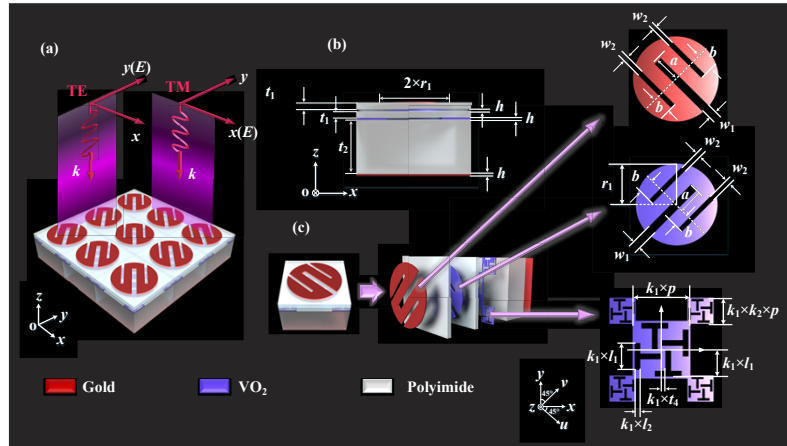
**Fig. 1.** Schematic views of the proposed MS as viewed from various angles: (a) array diagram illustrated with $3 \times 3$ periods, (b) the side view of the unit and (c) the structural decomposition of the unit.

boundary condition. To ensure that the *x*-polarized EMW is incident vertically on the proposed MS, the Floquet port is set above the resonant unit.

## 3. Results and discussion

### 3.1. *MS in low temperature (polarization converter)*

When the MS is at low temperature, the design consists of a top metal circular resonant patch and a bottom metal reflector, separated by a three-layer dielectric substrate; at this point, the structure features the polarization conversion function. The *u*-axis and *v*-axis can be derived when the *x*-axis and *y*-axis are deflected by 45° clockwise, respectively. Thus, when the EMW is polarized along the *x*-axis, the electric field vector of the incident wave ($E_{\text{inc}}$) can be decomposed in *u*- and *v*-axis directions as follow (where $i_u$ and $i_v$ denote the corresponding unit vectors):

$$E_{\text{inc}} = E_x i_x = E_u i_u + E_v i_v \tag{1}$$

The electric field vector of the reflected wave ($E_{\text{ref}}$) can be similarly decomposed and expressed in the form of the following matrix:

$$E_{\text{ref}} = \begin{pmatrix} i_u & i_v \end{pmatrix} \begin{pmatrix} r_{uu} & r_{uv} \\ r_{vu} & r_{vv} \end{pmatrix} \begin{pmatrix} E_u \\ E_v \end{pmatrix} \tag{2}$$

The above can be viewed in Fig. 2(a). In addition, since the resonant structures of the polarization conversion MSs are generally symmetrical along the *u*- and *v*-axis, the cross-polarized reflection coefficients are expressed in terms of $r_{vu}$ and $r_{uv}$ and are infinitely close to 0 in theory. By further derivation, Eq.(2) is transformed into the following form:

$$E_{\text{ref}} = E_x \cos(45°)(r_{uu} i_u + r_{vv} i_v) \tag{3}$$
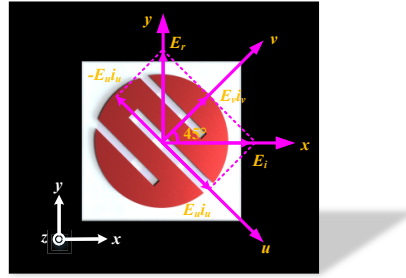
**Fig. 2.** Schematic representation of the incident and reflected polarized EMW.

The co-polarized reflection coefficients can be expanded and expressed as Eqs. (4) and (5). Moreover, the phase difference is defined as in Eq. (6):

$$\boldsymbol{r}_{uu} = |r_{uu}|e^{j\phi u} \tag{4}$$

$$\boldsymbol{r}_{vv} = |r_{vv}|e^{j\phi v} \tag{5}$$

$$\Delta\phi = \phi_{uu} - \phi_{vv} \tag{6}$$

If conditions (7) and (8) are both satisfied (where $n$ is the integer), the electric field vector of the reflected wave ($\boldsymbol{E}_{\mathrm{ref}}$) can be reduced to Eq. (9) eventually.

$$|\boldsymbol{r}_{uu}| = |\boldsymbol{r}_{vv}| = 1 \tag{7}$$

$$\Delta\phi = \pi + 2n\pi \tag{8}$$

$$\boldsymbol{E}_{\mathrm{ref}} = \boldsymbol{E}_x\cos(45°)e^{j\phi v}(\boldsymbol{i}_u + e^{j\Delta\phi}\boldsymbol{i}_v) = -\boldsymbol{E}_x e^{j\phi v}\boldsymbol{i}_y \tag{9}$$

The final result of Eq.(9) demonstrates that the electric field direction of the EMW undergoes the 90° conversion from the $x$-axis to the $y$-axis when the conditions mentioned above are met, i.e., the polarization conversion is generated.

The derivation of the above equation illustrates the generation of polarization conversion. In addition, several evaluative indicators need to be specified. A polarization conversion rate (PCR) greater than 90% is generally hoped for. In the study of reflective polarization conversion MSs, the values of the polarized transmission coefficients are 0. Therefore, the formula for PCR can be simplified as follows:

$$\mathrm{PCR} = \frac{r_{yx}^2}{r_{yx}^2 + r_{xx}^2} \tag{10}$$

where $r_{xx}$ and $r_{yx}$ are the co-polarized reflection coefficient and the cross-polarized reflection coefficient separately. Moreover, the operating band and relative bandwidth (*RB*) for PCR > 0.9 are defined in Eqs. (11) and (12) respectively, where the $f_{\mathrm{H}}$ and $f_{\mathrm{L}}$ respectively represent the highest and the lowest frequencies which the PCR over 90%.

$$\Delta f = f_{\mathrm{H}} - f_{\mathrm{L}} \tag{11}$$

$$RB = \frac{2 \times \Delta f}{f_{\mathrm{H}} + f_{\mathrm{L}}} \tag{12}$$

When VO$_2$ is at low temperature (the structure of VO$_2$ at low temperature is marked in white as follows), the proposed MS possesses the function of polarization conversion. In Fig. 3(a), the red curve denotes the cross-polarized reflection amplitude ($r_{yx}$) while the co-polarized reflection amplitude ($r_{xx}$) is depicted by the black dashed line. When the polarization conversion occurs, the

amplitude of $r_{xx}$ drops sharply, reaching the first resonance point at 0.73 THz, with an amplitude of 0.116. Following this, the resonance points with lower amplitudes of 0.012 and 0.030 occur at 0.90 THz and 1.25 THz, respectively. Meanwhile, the curve of $r_{yx}$ rises steeply, with amplitude above 0.8 in the range of 0.69 THz-1.38 THz. The phase difference and the co-polarized reflection amplitudes are described in Figs. 3(c) and (d) when the electric field directions of EMW are along the *u*-axis and the *v*-axis, respectively. In the range of 0.69 THz-1.38 THz, $r_{uu}$ and $r_{vv}$ curves whose values are approached 1 are closed to each other. According to the above derivation of the equations, in the lossless state, the values of $r_{uu}$ and $r_{vv}$ meet Eq.(7). However, since the proposed MS is lossy, $r_{uu} \approx r_{vv} \approx 1$ is considered to meet the conditions of the cross-polarization conversion. Also, within the above band, the phase difference ($|\Delta\varphi| < 180°\pm37°$) approximately satisfies Eq.(8). Take the data in Fig. 3(a) into Eqs. (10) and (18) to obtain the curves representing the PCR and absorptivity of this MS, as shown in Fig. 3(b). In 1.69 THz-1.38 THz, the PCR curve is above the standard line of 0.9, while the absorptivity remained low. It visualizes that when $VO_2$ is at low temperature, the proposed MS achieves the polarization conversion with the *RB* of 66.7%, and only a few of the reflected waves are absorbed, which indicates the characteristics of the low losses and high polarization conversion efficiency in the operating band.
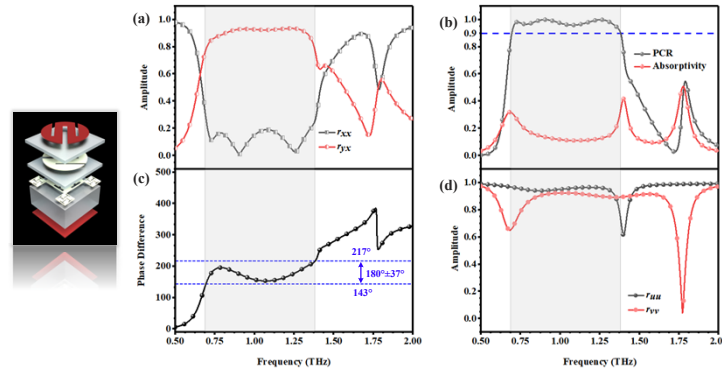


**Fig. 3.** The curves plots of polarization conversion MS when $VO_2$ is at low temperature: (a) the co-polarized reflection amplitude and cross-polarized reflection amplitude of incident EMW when the direction of electric field is along the *x*-axis, (b) the curves of PCR and absorptivity, (c) the phase difference and (d) the co-polarized reflection amplitude when the polarized direction of EMW are along the *u*- and *v*-axis respectively.

Surface currents provide a valuable illustration of the principle of polarization conversion. The surface currents at 0.73 THz and 0.90 THz are displayed in Fig. 4. The blue arrows indicate the directions of surface currents in the area where they are located, and their components along the *xoy* coordinate axis are marked by the black arrows. As exhibited in Fig. 4(a), the surface currents on the metal resonator are strongest at the three slots whose currents are in the same distribution at 0.73 THz. The two currents, $I_1$ and $I_2$, with particular strength at the middle slot, are in opposite directions and their components $I_{1y}$ and $I_{2y}$ on the *y*-axis are parallel to the currents in the bottom metal reflector as seen in Fig. 4(b). The electric resonance is generated by $I_{2y}$, which is in the same direction as the current on the metal reflector. In contrast, $I_{1y}$ which is opposite to the current on the metal reflector generates magnetic resonance. However, the components of the currents $I_1$ and $I_2$ on the *x*-axis are perpendicular to the currents on the bottom metal reflector, which have no significance for the generation of resonance. The resonances of the remaining two slots are identical to those described above and are therefore not described in detail. Overall, the 0.73 THz resonant frequency is caused by the electric and magnetic resonances combined. However, the current distribution at 0.90 THz merely produces magnetic resonance, which is different from 0.73 THz. In Fig. 4(c), both at the slots and the outer edge of the metal resonant

patch, the surface currents almost flow towards the -*u*-axis, opposite the currents on the bottom metal reflector. The loop currents are formed in the dielectric substrate layers. The magnetic dipole **m** and the magnetic field **H**, according to the right-hand rule, are created, where the magnetic field component $H_y$ parallel to the electric field **E** is essential for the cross-polarization of EMW.
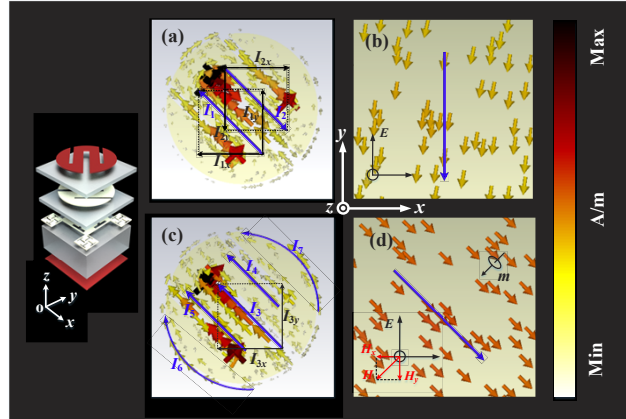


**Fig. 4.** Surface current diagrams: (a) surface currents on slotted circular metal resonant patches at 0.73 THz, (b) surface currents on metal reflector plates at 0.73 THz, (c) surface currents on slotted circular metal resonant patches at 0.90 THz, and (d) surface currents on metal reflector plates at 0.90 THz.

When the incidence direction of EMW deviates from the *z*-axis by the specified angles, the polarization conversion abilities for the proposed MS undergo specific changes. The PCR in the operating band is consistently above 0.9 during the increasing incidence angle to 33°, as displayed in Fig. 5. At incidence angles greater than 33°, a slight weakening of the polarization conversion occurs at 0.79 THz; the PCR is below 0.9 but still above 0.8 at this point. It is worth noting that as the increase of incidence angle, the operating band broadens somewhat at high frequencies, from $f_H = 1.38$ THz to $f_H = 1.41$ THz. Explain the deterioration of the polarization conversion effect at large angles of incidence from the view of the equations. When the electromagnetic wave is incident vertically on the MS, the propagation phase in the dielectric can be denoted as $2\beta = 2\sqrt{\varepsilon_r}k_0h$, where $\theta_t$ and $\varepsilon_r$ indicate the refraction angle and relative permittivity, respectively. However, when the electromagnetic wave is incident at a large angle, the propagation phase becomes to $2\beta = 2\sqrt{\varepsilon_r}k_0h/\cos\theta_t$. The destructive interference resulting from the additional propagation phase will break the original interference conditions. Therefore, the increasing rise of incident angle will deteriorate the polarization conversion [32].
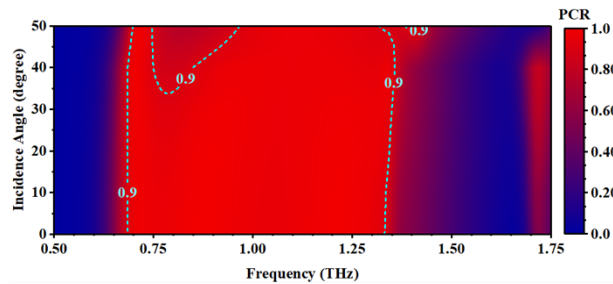


**Fig. 5.** Variation in PCR when the angle of incidence is increased.

From the top to the bottom, the thickness of the third-layer dielectric substrate for the proposed MS is noted as $t_2$. From Fig. 6(b), it can be seen that at $t_2 = 24$ μm, three resonant frequencies exist at 0.72 THz ①, 1.04 THz ②, and 1.35 THz ③, respectively. Since PCR > 0.9 can be transformed to $|\mathbf{r}_{xx}| < -10$ dB, the cross-polarization reflection amplitude greater than -10 dB in the range 0.75 THz-0.90 THz is the direct cause of the depressed PCR curve at low frequencies, as shown in Fig. 6(a). With the increase of $t_2$, frequencies ① and ② approach each other, resulting in the reduction of the reflection amplitude between the two mentioned frequencies, and the band with PCR < 0.9 is improved subsequently. At $t_2 = 28$ μm, the three frequencies interact with each other, creating the high PCR and ultra-broadband effect in the range of 0.69 THz-1.38 THz. However, during the continuous increase in $t_2$ to 32 μm, frequencies ① and ② merge into a single frequency, thus weakening the polarization conversion effect. Besides, frequency ③ generates the redshift that narrows the operating bandwidth. Figures 6(c) and (d) depict the effect of the variation in the radius of the metallic circular resonant patch on $r_{xx}$ and the PCR. Under the impact of the metallic resonant patch with $r_1 = 22$ μm, the resulting resonance points are located at 0.83 THz (marked by ④ in Fig. 6(d)) and 1.14 THz, respectively. The resonance point situated at 1.14 THz affects a wide range of frequencies, and as $r_1$ increases to 23.5 μm, the resonance point splits into two, which are noted as frequencies ⑤ and ⑥ accordingly. The increasing $r_1$ causes a significant red shift in frequencies ④ and ⑤, while the blue shift in frequency ⑥ is relatively small. At $r_1 = 28$ μm, powerful resonances occur at frequencies ⑤ and ⑥, with $r_{xx}$ reaching -44.7 dB and -47.7 dB, respectively, whose PCR is almost 100%. Multiple frequencies and appropriate distance between frequencies are generally two critical factors in maintaining a high PCR and the wide band. However, frequencies ⑤ and ⑥ are getting further apart due to frequency shifts, resulting in $|r_{xx}| > -10$ dB between the two points, which is reflected in the PCR curve as a depression at the mid frequencies. Combining the bandwidth and PCR performance indicators, $r_1 = 25$ μm is chosen as the optimal value, at which point the proposed MS enables more than 90% PCR within 0.69 THz - 1.38 THz.
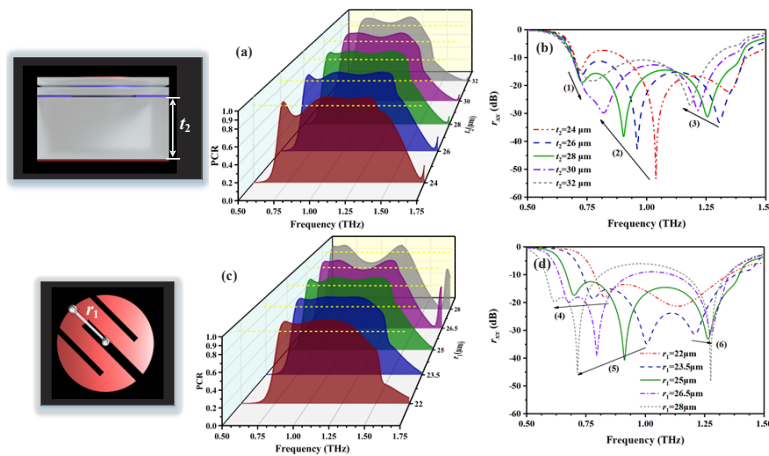


**Fig. 6.** The change in the PCR and co-polarized reflectance with the variations in the structural parameters: (a) PCR changes with $t_2$, (b) $\mathbf{r}_{xx}$ changes with $t_2$, (c) PCR changes with $r_1$, and (d) $\mathbf{r}_{xx}$ changes with $r_1$.

## 3.2.  *MS in high temperature (absorber)*

In high temperatures, the MS characterized the absorption function consists of two circular structures with staggered slots in metal and VO$_2$, a VO$_2$ rectangular resonant patch with the "T" shaped slotted structures, and three layers of the dielectric substrate and a metal reflector.

Assuming that EMW is incident from port 1 and transmitted from port 2 of the MS as presented in Fig. 7, the reflectance and transmittance of the MS can be expressed in terms of the **S**-parameter as:

$$R(\omega) = |S_{11}|^2 \tag{13}$$

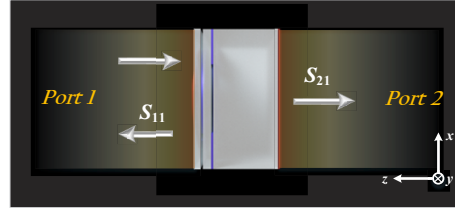$$T(\omega) = |S_{21}|^2 \tag{14}$$



**Fig. 7.** Schematic representation of the *S*-parameters.

Define the absorptivity of the MS as:

$$A(\omega) = 1 - R(\omega) - T(\omega) \tag{15}$$

If the perfect absorption of electromagnetic waves by the MS is desired, then it is necessary to make $R(\omega)=T(\omega)=0$. Thus, the perfect absorption can be achieved by adjusting $S_{11}$ and $S_{21}$. $d$ represents the thickness of the MS which is significant to the dispersion-free [34], $k=\omega/c$ is the transmitted wave number, $n = n_1 + in_2$ and $z = z_1 + iz_2$ describe the refractive index and impedance, respectively. At this point, $S_{21}$ can be expressed as Eq.(16) [35]:

$$S_{21}^{-1} = \left[ \sin(nkd) - \frac{i}{2}\left(z + \frac{1}{z}\right)\cos(nkd) \right] e^{ikd} \tag{16}$$

The complex refractive index and complex impedance can also be represented in the following form:

$$n(\omega) = \sqrt{\varepsilon(\omega)\mu(\omega)} \tag{17}$$

$$z(\omega) = \sqrt{\mu(\omega)/\varepsilon(\omega)} \tag{18}$$

Moreover, by adjusting the structure of the MS and its dimensions, the impedance can be made to match the free space theoretically perfectly, i.e., $z = 1$. $\varepsilon$ and $\mu$ should be equal to ensure that the reflected electromagnetic waves from the MS are zero, i.e., that the waves all enter the MS. At the same time, the MS should also possess significant losses, i.e., $n_2$ approaching infinity. At this point, $R(\omega)=T(\omega)=0$, then $A(\omega)=1$ achieves perfect absorption of the electromagnetic wave. The specific formulas [36] are derived as follows:

$$R(\omega) = |S_{11}|^2 = \left[ \frac{z(\omega)-1}{z(\omega)+1} \right]^2_{z(\omega)=1} = 0 \tag{19}$$

$$T(\omega) = |S_{21}|^2 = \lim_{n_2\to\infty}(e^{-i(n_1-1)kd}e^{n_2kd}) = \lim_{n_2\to\infty} e^{-2n_2kd} = 0 \tag{20}$$

In the analysis of impedance matching, the *S*-parameter can be used for representation:

$$z = \pm\sqrt{\frac{(1+S_{11})^2 - S_{21}{}^2}{(1-S_{11})^2 - S_{21}{}^2}} \tag{21}$$

If the bottom of the MS is the metal reflector, then $S_{21} = 0$.

When $VO_2$ is at a specific high temperature (the structure of $VO_2$ at high temperature is marked in blue as follow), the proposed MS possesses the absorption effect on incident EMW. As can be seen from the previous equations on EMW absorption, the ideal impedance matching is essential for the absorptivity to approach 100%. Figure 8(a) depicts the absorptivity curve of the presented MS and Fig. 8(b) is the complex impedance diagram. It is clear from Fig. 8(a) that the MS can absorb over 90% of the EMW in the range of 0.67 THz-0.95 THz in both TE and TM modes. Absorptivity reaches the maximum of 97% at 0.80 THz. Furthermore, in the above operating band, the real part of the impedance $z$ (Re) approximates 1, and the imaginary part (Im) is close to 0. Moreover, at 0.80 THz, Re = 1.11, Im = 0.28. The sum of the reflected amplitudes in Fig. 8(c) is the amplitude of $S_{11}$, which is taken into Eqs. (13) and (15), resulting in the absorptivity. The amplitude of $r_{xx}$ decreases rapidly in the range of 0.67 THz-0.95 THz, while the amplitude of $r_{yx}$ remains stable at less than 0.1. This demonstrates that the MS offers an efficient absorption effect in the operating band, and the polarization effect is eliminated mainly due to the structure's unique design.
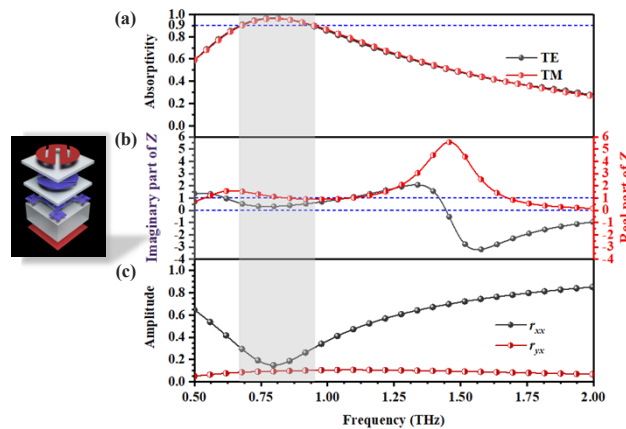


**Fig. 8.** (a) The absorptivity curves of the proposed MS in TE and TM modes, (b) the normalized complex impedance $z$ of the proposed MS, and (c) the reflection amplitude curves.

To illustrate the role of the $VO_2$ resonant patches, the circular and rectangular resonant patches are removed from the proposed MS individually, and the total thickness of the dielectric substrate remains unchanged; the absorptivity curves are presented in Fig. 9. The simulation results indicate that the significant absorption effect on the EMW is the rectangular resonant patch with the "T" slotted structure, which reaches the maximum value of 0.89 at 0.95 THz. However, the $VO_2$ circular resonant patch weakens the polarization conversion effect of the top metal resonant patch by rotating it 90° clockwise. When the rectangular resonant patch is not incorporated, the MS attains an absorptivity of just 56% at 0.84 THz, which can be superimposed on the effect achieved by the rectangular resonant patch described above. Eventually, 97% absorptivity can be obtained at 0.80 THz.

The qualitative analysis of the equivalent circuit for the proposed MS is presented. It can be found that the three-layer resonant patches in the proposed MS can be grouped into two parts. The metal and $VO_2$ circular resonant patches with staggered slots belong to part 1, and the rectangular resonant patch with a "T" slot structure is named part 2. The equivalent circuit of part 1 is shown in Fig. 10(a), where $L_1$ is the self-inductance of the metal circular resonant patches, $C_1$ is the gap capacitance of the metal circular resonant patches, and $R_1$ represents the resistance (resistance means the loss which includes the ohmic and radiation loss). Similarly, the self-inductance, gap capacitance, and resistance of $VO_2$ circular resonant patches with staggered
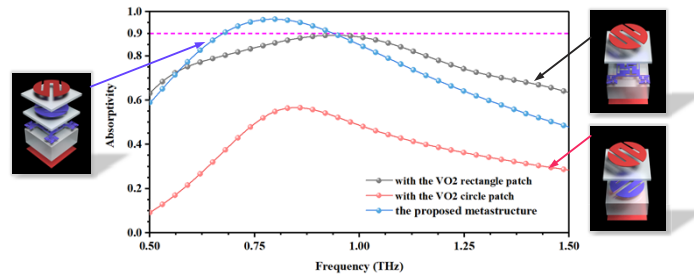
**Fig. 9.** The absorptivity of three structures used to explain the role of the VO$_2$ resonant patches.

slots are denoted by $L_2$, $C_2$, and $R_2$, respectively [37]. As the structure of the VO$_2$ circular resonant patch differs from the metal circular resonant patch merely in the direction of the slots, the two remain uniform in terms of the circuit arrangement. In addition, the coupling capacitance $C_{m1}$ is used to reflect the coupling effect between the two circular resonant patches. The third layer resonant patch is the combination of a rectangular resonant patch with a "T" slot structure and four proportionally scaled down patches, which belong to the scaling topology type structure, the equivalent circuit as shown in Fig. 10(b). The self-inductance $L_3$, gap capacitance $C_3$, and resistance $R_3$ of the VO$_2$ rectangular patch in the middle form a series circuit, which is connected in parallel with the self-inductance $L_4$, gap capacitance $C_3$, and resistance $R_4$ of the four VO$_2$ rectangular patches surrounding it, forming the equivalent circuit of part 2 [38]. However, the whole can be simplified to a series circuit of $L_{eqv}$, $C_{eqv}$ and $R_{eqv}$. Similarly, the coupling effect between part 1 and part 2 is represented by the coupling capacitance $C_{m2}$. Ultimately, Fig. 10(c) can mean the qualitative equivalent circuit of the proposed MS in the absorption state. As the MS described has no transmission coefficient, a conventional two-port network is effectively a single-port network. Complex single-port networks, however, can eventually be reduced to *RLC* series resonant circuits.
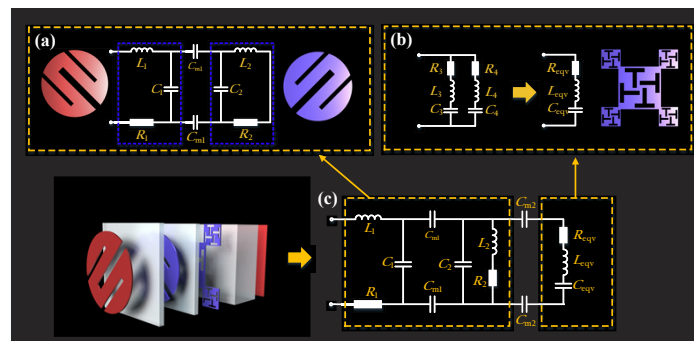


**Fig. 10.** The equivalent circuit models of the (a) the metal and VO$_2$ resonant patches, (b) the rectangular resonant patch with a "T" slot structure, and (c) the whole unit at 68°C.

After simplifying the complex circuit in Fig. 10(c), the quantitative analysis of the equivalent circuit will be carried out. It can be observed that the MS creates an effective absorption at 0.80 THz due to the combined effect of the bottom metal reflector, three resonant layers, and the dielectric substrate. The black curve illustrates the $S_{11}$ simulated by HFSS in Fig. 11(b), while the red curve describes the theoretical circuit fitting whose equivalent circuit model is presented in Fig. 11(a). $\boldsymbol{R} = 281.1$ ohm, $\boldsymbol{L} = 97$ pH, and $\boldsymbol{C} = 0.000408$ pF are selected in series to match the

impedance of the free space, the $S_{11}$ simulation curve displays high similarity to the theoretical circuit curve and hence attains the desired absorption effect.
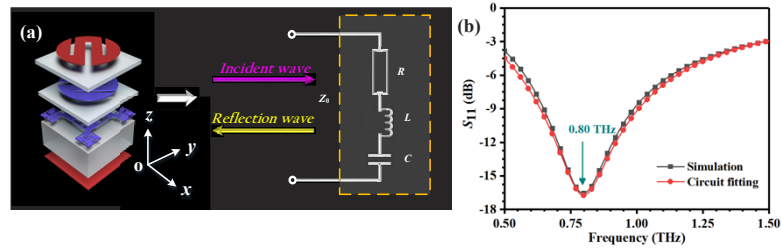


**Fig. 11.** (a) The equivalent circuit model of the proposed MS at 68°C, and (b) the theoretical circuit fitting and the $S_{11}$ simulation curves.

When the MS works at 0.80 THz, the power loss density distributions on the three resonance layers in the absorption state are described in Figs. 12(a), (b) and (c), respectively. From Fig. 12(a), it can be observed that the power loss is concentrated in the dielectric substrate at the edges of the circular metal resonator, especially in areas 1 and 2. In Fig. 12(b), the power loss at the edges of the circular VO$_2$ resonators (corresponding to the mentioned areas 1 and 2) remains at a high value. Besides, energy loss also occurs in areas 3 and 4. In the third resonant layer, four small rectangular resonant patches, especially their "T" shaped slotted structures, play an essential role in the power loss. Meanwhile, areas 5 and 6, corresponding to areas 1 and 2, still hold a high power loss. Overall, the excellent absorption effect maintained in 0.80 THz is attributed to the dielectric substrate under the influences of the three resonant patches and the loss characteristics of the VO$_2$ units in the proposed MS.
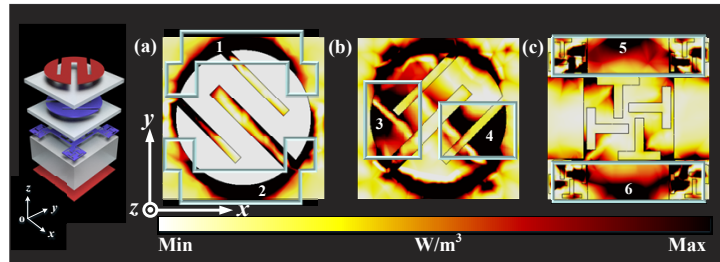


**Fig. 12.** The power loss density distributions at 0.80 THz: (a) on the layer of the circular metal resonant patch, (b) on the layer of the circular VO$_2$ resonant patch, and (c) on the layer of the rectangular resonant patch with the "T" shaped slotted structures.

The stability of the absorptivity at different polarization angles and incidence angles (described in Fig. 13 and Fig. 14, separately) shows the device's adaptability to complex environments to some extent. Figures 13(a) and (b) depict the variations in absorptivity and $S_{11}$ when the polarization angle is changed from 0° to 360° with a span of 30°, respectively. It can be noticed that $S_{11}$ is not entirely equivalent when the polarization angle changes, the reason being that the resonant structure is not centrosymmetric. At polarization angles of 60° and 240°, $S_{11}$ reaches a minimum value of 0.04 at 0.77 THz. However, the visible difference in $S_{11}$ is slight for the absorptivity. White dashed lines mark the band in Fig. 13(a) with absorptivity above 0.9, and it can be found that the operating band is noticeably changed only at low frequencies. In terms of structure and principle, the proposed MS adopts a polarization-canceling design scheme rather than the conventional symmetrical structure that triggers absorption. As a result, there is a slight difference in the absorption of waves at different polarization angles. Still, at the same time, it

results in a more significant absorption effect and a broader bandwidth. Besides, the case of the different incidence angles is presented in Fig. 14. as the angle of incidence increases, the operating band is reduced at both low and high frequencies, and the absorptivity is below 0.9 at incidence angles above 40°.
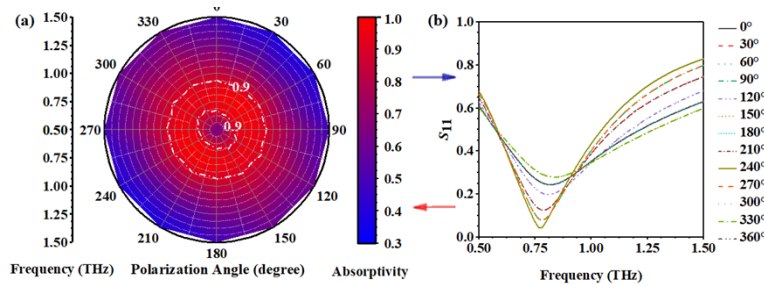


**Fig. 13.** (a) The absorption spectra of this MS varies with the polarization angle, and (b) the $S_{11}$ varies with the polarization angle.
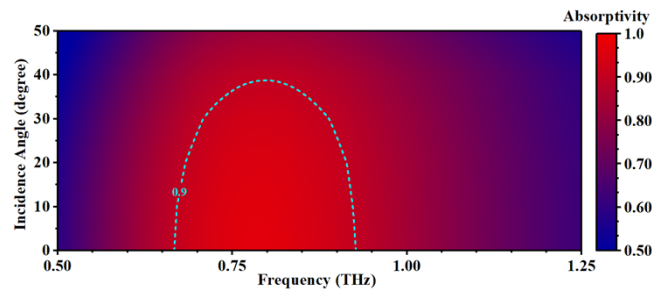


**Fig. 14.** Variation in absorptivity when the angle of incidence is increased.

As mentioned before, the thickness of the third dielectric substrate impacts the polarization conversion efficiency. In addition, $S_{11}$ experiences redshifts due to an increase in $t_2$, accompanied by a decrease in the amplitude of $S_{11}$. Specifically, its center frequency shifted from 0.90 THz to 0.74 THz, while the amplitude of $S_{11}$ decreased by 1.02 dB, as indicated in Fig. 15(a). As a result of the above, the absorptivity of the proposed MS increases and shifts to the lower frequencies, as depicted in Fig. 15(b). However, as the variation of $t_2$ affects both PCR and absorptivity performance indicators, $t_2 = 28\,\mu m$ is set as the optimal value on balance. The parameter $k_2$, which represents the scaling ratio, causes $S_{11}$ first to decrease and then to increase, as shown in Fig. 15(d), where $S_{11}$ reaches the minimum value of -24.6 dB at $k_2 = 0.4$ and increases again to -12.3 dB at $k_2 = 0.45$. However, when evaluated in terms of absorptivity, the difference between the two is only approximately 1%, and the operating band is broadened at high frequencies at $k_2 = 0.45$, as seen in Fig. 15(c); therefore, $k_2 = 0.45$ is chosen as the optimum value. The given MS achieves an absorptivity of over 90% in the range of 0.67 THz - 0.95 THz. In summary, changing the parameter value thus leads to variations in the absorptivity; this phenomenon occurs mainly because of the impedance change. From the perspective of the equation, the difference in the parameter value leads to variation in $S_{11}$, which, according to Eq. (21), will directly affect the impedance value when not having the transmission coefficient. From the perspective of the circuit, changing the structure will affect the value of the $RLC$ taken in its equivalent circuit, thus affecting the effect of matching the free-space impedance. Therefore, selecting appropriate values for the structural parameters is critical to the performance of the MS.
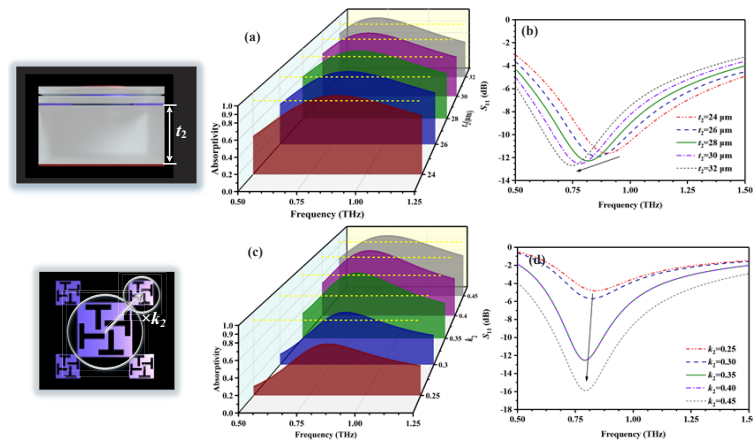
**Fig. 15.** The change in the absorbtivity and $S_{11}$ with the variations in the structural parameters: (a) absorbtivity changes with $t_2$, (b) $S_{11}$ changes with $t_2$, (c) absorbtivity changes with $k_2$, and (d) $S_{11}$ changes with $k_2$.

## 4. Conclusion

In summary, based on the phase transition characteristics of $VO_2$, a multifunctional MS that enables the ultra-broadband polarization conversion and narrowband absorption is proposed in this paper. The functions are switched by controlling the operating temperature. At the high temperature, the proposed MS can absorb more than 90% of EMW in 0.67 THz - 0.95 THz. At low temperatures, the proposed MS can cross-polarize EMW in the range of 0.69 THz-1.38 THz, and its PCR can be maintained at more than 90% in the operating band, reaching 98% at 0.73 THz and close to 100% at 0.90 THz as well as 1.25 THz. This multifunctional MS can be applied to the communication system of 6G, temperature-controlled system, stealth technology, and so on.

**Disclosures.** The authors declare no conflicts of interest.

**Data availability.** Data underlying the results presented in this paper are not publicly available at this time but may be obtained from the authors upon reasonable request.

## References

1. J. Zhang, J. C. Zhang, X. F. Shuai, and R. H. Zhao, "Design and synthesis strategies: 2D materials for electromagnetic shielding/absorbing," Chem. Asian J. **16**(23), 3817–3832 (2021).
2. Z. Y. Zhou and J. Huang, "Target head direction far field radar cross section reduction based on narrow surface element method," Optik **200**, 163230 (2020).
3. Q. Y. Zhang and Y. Gao, "A compact broadband dual-polarized antenna array for base stations," Antennas Wirel. Propag. Lett. **17**(6), 1073–1076 (2018).
4. L. Guan, Z. He, D. Z. Ding, Y. F. Yu, W. Zhang, and R. S. Chen, "Polarization-controlled shared-aperture metasurface for generating a vortex beam with different modes," IEEE Trans. Antennas Propagat. **66**(12), 7455–7459 (2018).
5. S. J. Zhang, Z. W. Li, and F. Xing, "Review of polarization optical devices based on graphene materials," Int. J. Mol. Sci. **21**(5), 1608 (2020).
6. G. B. Xavier, G. Vilela de Faria, G. P. Temporão, and J. P. von der Weid, "Full polarization control for fiber optical quantum communication systems using polarization encoding," Opt. Express **16**(3), 1867–1873 (2008).
7. S. Y. Wu, J. P. Zhao, and J. Xu, "A circularly polarized low-profile magnetoelectric dipole antenna," Microw. Opt. Techn. Let. **63**(11), 2852–2858 (2021).
8. P. F. Qiao, W. J. Yang, and C. J. C. Hasnain, "Recent advances in high-contrast metastructures, metasurfaces, and photonic crystals," Adv. Opt. Photon. **10**(1), 180–245 (2018).
9. H. R. Chen, Y. Z. Cheng, J. C. Zhao, and X. S. Mao, "Multi-band terahertz chiral metasurface with giant optical activities and negative refractive index based on T-shaped resonators," Mod. Phys. Lett. B **32**(30), 1850366 (2018).

10. O. Akgol, E. Unal, and O. Altintas, "Design of metasurface polarization converter from linearly polarized signal to circularly polarized signal," Optik **161**, 12–19 (2018).
11. F. Chen, Y. Cheng, and H. Luo, "Temperature tunable narrow-band terahertz metasurface absorber based on InSb micro-cylinder arrays for enhanced sensing application," IEEE Access **8**, 82981–82988 (2020).
12. H. B. Wang, Y. J. Cheng, and Z. N. Chen, "Dual-band miniaturized linear-to-circular metasurface polarization converter with wideband and wide-angle axial ratio," IEEE Trans. Antennas Propagat. **69**(12), 9021–9025 (2021).
13. R. Dutta, J. Ghosh, and Z. Yang, "Multi-band multi-functional metasurface-based reflective polarization converter for linear and circular polarizations," IEEE Access **9**, 152738–152748 (2021).
14. Y. Li, J. Lin, H. J. Guo, W. J. Sun, S. Y. Xiao, and L. Zhou, "A tunable metasurface with switchable functionalities: from perfect transparency to perfect absorption," Adv. Opt. Mater. **8**(6), 1901548 (2020).
15. H. J. Zhang, Y. Liu, Z. Q. Liu, X. S. Liu, G. Q. Liu, G. L. Fu, J. Q. Wang, and Y. Shen, "Multi-functional polarization conversion manipulation via graphene-based metasurface reflectors," Opt. Express **29**(1), 70–81 (2021).
16. R. Zhang, B. You, S. C. Wang, K. Han, X. P. Shen, and W. H. Wang, "Broadband and switchable terahertz polarization converter based on graphene metasurfaces," Opt. Express **29**(16), 24804–24815 (2021).
17. Q. Y. Wen, H. W. Zhang, Q. H. Yang, Z. Chen, Y. Long, Y. L. Jing, Y. Lin, and P. X. Zhang, "A tunable hybrid metamaterial absorber based on vanadium oxide films," J. Phys. D: Appl. Phys. **45**(23), 235106 (2012).
18. L. Lei, F. Lou, K. Y. Tao, H. X. Huang, X. Cheng, and P. Xu, "Tunable and scalable broadband metamaterial absorber involving VO2-based phase transition," Photonics Res. **7**(7), 734–741 (2019).
19. Y. Zhao, Q. P. Huang, H. L. Cai, X. X. Lin, and Y. L. Lu, "A broadband and switchable VO2-based perfect absorber at the THz frequency," Opt. Commun. **426**, 443–449 (2018).
20. H. Takami, K. Kawatani, and T. Kanki, "High temperature-coefficient of resistance at room temperature in w-doped vo2 thin films on al2o3 substrate and their thickness dependence," Jpn. J. Appl. Phys. **50**(5R), 055804 (2011).
21. R. Basu, V. Srihari, and M. Sardar, "Probing phase transition in VO2 with the novel observation of low-frequency collective spin excitation," Sci. Rep. **10**(1), 1–11 (2020).
22. D. Yan, M. Meng, and J. Li, "Vanadium dioxide-assisted broadband absorption and linear-to-circular polarization conversion based on a single metasurface design for the terahertz wave," Opt. Express **28**(20), 29843–29854 (2020).
23. Y. Qiu, D. X. Yan, and Q. Y. Feng, "Vanadium dioxide-assisted switchable multifunctional metamaterial structure," Opt. Express **30**(15), 26544–26556 (2022).
24. Q. Y. Feng, D. X. Yan, and X. J. Li, "Realization of absorption, filtering, and sensing in a single metamaterial structure combined with functional materials," Appl. Opt. **61**(15), 4336–4343 (2022).
25. L. Chen and Z. Song, "Simultaneous realizations of absorber and transparent conducting metal in a single metamaterial," Opt. Express **28**(5), 6565–6571 (2020).
26. M. Li, S. Magdassi, Y. F. Gao, and Y. Long, "Hydrothermal synthesis of VO2 polymorphs: advantages, challenges and prospects for the application of energy efficient smart windows," Small **13**(36), 1701147 (2017).
27. M. Tahir, "Hierarchical 3D VO2/ZnV2O4 microspheres as an excellent visible light photocatalyst for CO2 reduction to solar fuels," Appl. Surf. Sci. **467–468**, 1170–1180 (2019).
28. D. Gu, X. Zhou, and Z. Sun, "Influence of Gadolinium-doping on the microstructures and phase transition characteristics of VO2 thin films," J. Alloys Compd. **705**, 64–69 (2017).
29. Y. Z. Cheng, H. L. Zhao, and C. Li, "Broadband tunable terahertz metasurface absorber based on complementary-wheel-shaped graphene," Opt. Mater. **109**, 110369 (2020).
30. Q. H. Zhou, P. G. Liu, L. A. Bian, C. X. Liu, and G. H. Cheng, "Controlling enhanced absorption in graphene metamaterial," Opt. Commun. **413**, 310–316 (2018).
31. T. L. Wang, H. Y. Zhang, Y. Zhang, Y. P. Zhang, and M. Y. Cao, "Tunable bifunctional terahertz metamaterial device based on Dirac semimetals and vanadium dioxide," Opt. Express **28**(12), 17434–17448 (2020).
32. H. Zhang, X. He, D. Zhang, and H. F. Zhang, "Multitasking device with switchable and tailored functions of ultra-broadband absorption and polarization conversion," Opt. Express **30**(13), 23341–23358 (2022).
33. T. Lv, G. Dong, and C. Qin, "Switchable dual-band to broadband terahertz metamaterial absorber incorporating a VO₂ phase transition," Opt. Express **29**(4), 5437–5447 (2021).
34. D. R. Smith, D. C. Vier, and T. Koschny, "Electromagnetic parameter retrieval from inhomogeneous metamaterials.," Phys. Rev. E **71**(3), 036617 (2005).
35. H. Wu, S. Ji, and J. Zhao, "Design and Analysis of a Triple-band Non-zonal Polarization Electromagnetic Metamaterial Absorber," ACES **36**(6), 697–706 (2021).
36. S. C. Jiang, X. Xiong, and Y. S. Hu, "Controlling the polarization state of light with a dispersion-free metastructure," Phys. Rev. X **4**(2), 021026 (2014).
37. Y. G. Zhang, J. B. Wu, and L. J. Liang, "Effect of loss and coupling on the resonance of metamaterial: An equivalent circuit approach," Sci. China Inf. Sci. **57**(12), 1–8 (2014).
38. R. Mishra and R. Panwar, "Investigation of graphene fractal frequency selective surface loaded terahertz absorber," Opt. Quantum Electron. **52**(6), 317 (2020).